Brief of specific publications 1

pubs.acs.org/Biomac

Article

Multibiofunctional Self-healing Adhesive Injectable Nanocomposite Polysaccharide Hydrogel

Pritiranjan Mondal and Kaushik Chatterjee*

Cite This: *Biomacromolecules* 2024, 25, 4762−4779

Read Online

ACCESS | Metrics & More | Article Recommendations | Supporting Information

ABSTRACT: Injectable hydrogels with good antimicrobial and antioxidant properties, self-healing characteristics, suitable mechanical properties, and therapeutic effects have great practical significance for developing treatments for pressing healthcare challenges. Herein, we have designed a novel, self-healing injectable hydrogel composite incorporating cross-linked biofunctional nanomaterials by mixing alginate aldehyde (Ox-Alg), quaternized chitosan (QCS), adipic acid dihydrazide (ADH), and copper oxide nanosheets surface functionalized with folic acid as the bioligand (F-CuO). Gelation was achieved under physiological conditions via the dynamic Schiff base cross-linking mechanism. The developed nanocomposite injectable hydrogel demonstrated the fast self-healing ability essential to bear deformation and outstanding antibacterial properties along with ROS scavenging ability. Furthermore, the optimized formulation of our F-CuO-embedded injectable hydrogel exhibited excellent cytocompatibility, blood compatibility, and *in vitro* wound healing performance. Taken together, the F-CuO nanosheet cross-linked injectable hydrogel composite presented herein offers a promising candidate biomaterial with multifunctional properties to develop solutions for addressing clinical challenges.

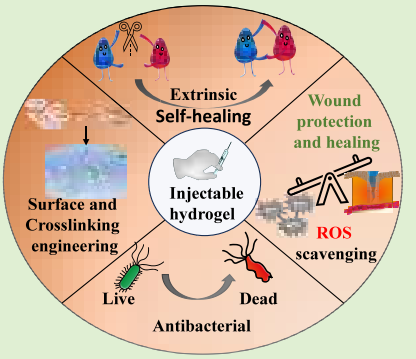

1. INTRODUCTION

In recent years, hydrogels have gained research interest as potent biomaterials in healthcare due to their excellent biocompatibility, good permeability, and ability to closely mimic the natural extracellular matrix (ECM).[1−5] However, their clinical uptake has been limited by various limitations of the current generation of hydrogels. For example, hydrogels can be tailored to support cell transplantation or engraftment[6] but necessitate physical placement in patients during invasive surgical procedures, which are associated with complications, risks of infection, patient discomfort, pain, and high medical costs.[7] Injectable hydrogels offer numerous advantages over conventional hydrogels in numerous applications. Injectable hydrogels can rapidly take the shape of any irregular cavities when dispensed via a minimally invasive delivery module.[8,9] They can be placed precisely in specific and deep locations via syringe/catheter without complex surgeries.

A widely adopted approach to engineer an injectable hydrogel is designing precursor prepolymer solutions that can undergo rapid chemical cross-linking to yield gels such that various therapeutic agents (drugs, proteins, cells, nanoparticles, etc.) can be homogeneously mixed into the precursor polymer solution in a potentially cargo-protective manner before administration.[10,11] However, sol-to-gel transition time is a critical parameter for clinical administration because rapid cross-linking may lead to syringe/catheter obstruction before the hydrogel is dispensed. In contrast, a delayed cross-linking process may result in material dissipation upon injection and the undesired release of unreacted precursors out of the target zone, leading to off-site cytotoxicity.[10,11] To overcome these challenges, the innovation of new hydrogels that can flow upon introducing shear stress (i.e., shear-thinning) and reform after stress removal (i.e., self-healing) has grown in popularity.[12] Apart from this, the placed hydrogels would continuously sustain external force in daily life once concerned for tissue engineering, which usually causes the traditional hydrogels to break, followed by function loss.

Furthermore, the damage to the hydrogel can also be accessible as a gateway for microbial invasion, resulting in a high chance of infection. In these circumstances, a self-healing hydrogel exhibiting antibacterial properties would be highly beneficial to inhibit bacterial infection at the wound site. Therefore, self-healing hydrogels using different reversible interactions, such as host−guest interaction,[13,14] hydrogen bond,[15,16] coordinate bond,[17,18] and charge interaction,[19,20] were developed to offer several advantages.[21] However, a multifunctionalized injectable hydrogel that synchronously performs on self-healing ability and on-demand antibiosis still has not been realized, which would have extensive potential in numerous bioengineering applications.

Received: January 5, 2024
Revised: May 29, 2024
Accepted: June 20, 2024
Published: July 11, 2024

Scheme 1. (a) Synthesis Scheme of QCS from Chitosan (CS), (b) Synthesis Scheme of Ox-Alg from Alginate (Alg), (c) Schematic Demonstration for Fabrication of the F-CuO/Ox-Alg/QCS Injectable Hydrogel. Digital Image of (d) Ox-Alg/QCS NH, (e) CuO/Ox-Alg/QCS NH (Red Arrows Indicate the Non-Homogeneous Distribution of CuO Nanosheet in the Hydrogel), (f) F-CuO/Ox-Alg/QCS NH. Scale Bar = 1 cm

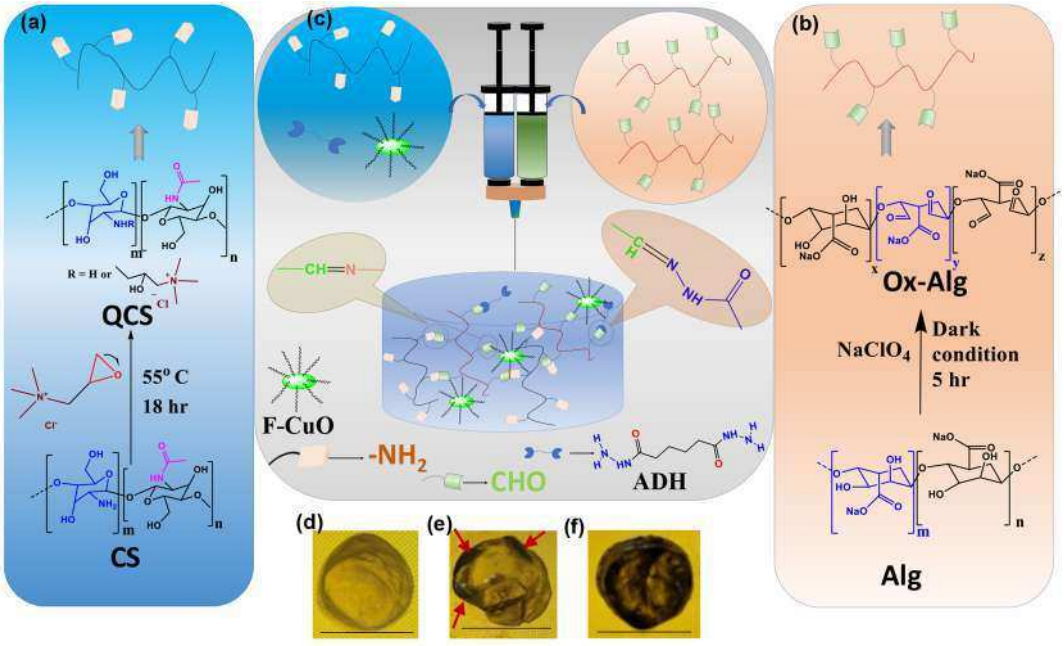

nanosheets. The bands at 3449 cm^{-1} belong to the asymmetric stretching vibrational mode of the O−H bond of absorbed water. Additionally, the optical property of synthesized CuO nanosheets was examined by UV−vis spectrophotometer (Figure S2, SI). The typical UV−vis spectrum of CuO nanosheet demonstrates an excitation band at ≈365 nm and ≈297 nm.[44]

After successfully synthesizing CuO nanosheets, they were modified with folic acid ligands via ligand-to-metal charge transfer at basic pH (Figure 1 c). The motivation for the modification was multifold, as follows: (1) enhance the dispersion of CuO nanosheets in an aqueous medium (Figure 1 g), (2) decrease the cytotoxicity of CuO nanosheets, (3) enable uniform distribution of CuO nanosheets within the hydrogel with cross-linking chemistry, and (4) facilitate interactions with folic receptors of cancer cells in case of use nanomaterials for anticancer activity for drug delivery and/or photothermal effect. The XRD pattern of the F-CuO is similar to the CuO phase but has a broad peak in the range of 11° to 17°, indicating the conjugation of folic acid to CuO nanosheets (Figure 1 b). Raman signal of F-CuO does not significantly differ from CuO (Figure 1d). The FTIR study further confirmed folic acid interaction with CuO nanosheet. FTIR spectra of F-CuO showed that there was no covalent conjugation of folic acid with CuO nanosheets but rather ionic interactions between them. The absorbance at 1681 cm^{-1}, 1505 cm^{-1}, 1180 cm^{-1}, and 769 cm^{-1} indicated the successful modification of folic acid molecules onto CuO nanosheets' surface (Figure 1e). This conjugation was further confirmed by UV = vis spectroscopy and Zeta potential measurements. The characteristic absorbance of the F-CuO nanosheet shifted to ≈352 nm, indicating the interaction between folic acid and CuO (Figure S2, SI). Zeta potential measurements showed that the surface zeta potential values of CuO and F-CuO are 14.1 mV and −38.2 mV, respectively (Figure 1f). The increased negative value in zeta potential value indicates the interaction of Folic acid on the surface of CuO nanosheets. The negatively charged carboxyl group in the folic acid at basic pH is easily conjugated with positively charged Cu in CuO nanosheets through ligand-to-metal charge transfer. These measurements confirmed the successful modification of the surface of CuO nanosheets by the attraction of the carboxyl group of Folic acid.

Cytotoxicity of the CuO nanosheets was evaluated by MTT assay against L929 fibroblast and HaCaT keratinocyte cells exposed to systematically varied concentrations of the nanomaterials. Cytotoxicity decreased markedly when the CuO nanosheet was modified with folic acid (Figure 1 (h, (i)). Since more than 50% of cells are viable when directly exposed to 0.125 mg/mL of F-CuO nanosheets, we used 0.1 mg/mL F-CuO nanosheet concentration in hydrogel for further studies.

Notably, this approach to surface functionalize nanomaterials with folic acid as a bioligand is generic and can be implemented for other metallic nanomaterials. We synthesized ZnO nanoflowers, functionalized them with folic acid, and characterized the modification to further demonstrate the broad application of this approach to other nanomaterials (Figures S3 and S4, SI). The yield of ZnO nanoflowers synthesis is 91 to 95%.

3.2. Preparation and Characterizations of Hydrogels.

Positively charged quaternized chitosan (QCS) was synthesized using glycidyl trimethylammonium chloride (GTMAC) as an etherifying agent in deionized water under acidic conditions. In an acidic aqueous medium, the epoxy rings of GTMAC conjugations mostly predominantly occur with the amine group of the chitosan backbone[45,46] (Schematic 1a). This functionalization of the chitosan was confirmed by ^{1}H NMR and FTIR. A strong peak at ≈ δ 3.17 ppm was observed, demonstrating the presence of methyl groups in the quaternary ammonium side chains ($-N^+(CH_3)_3$) (Figure 2b). The

https://doi.org/10.1021/acs.biomac.4c00016
Biomacromolecules 2024, 25, 4762−4779

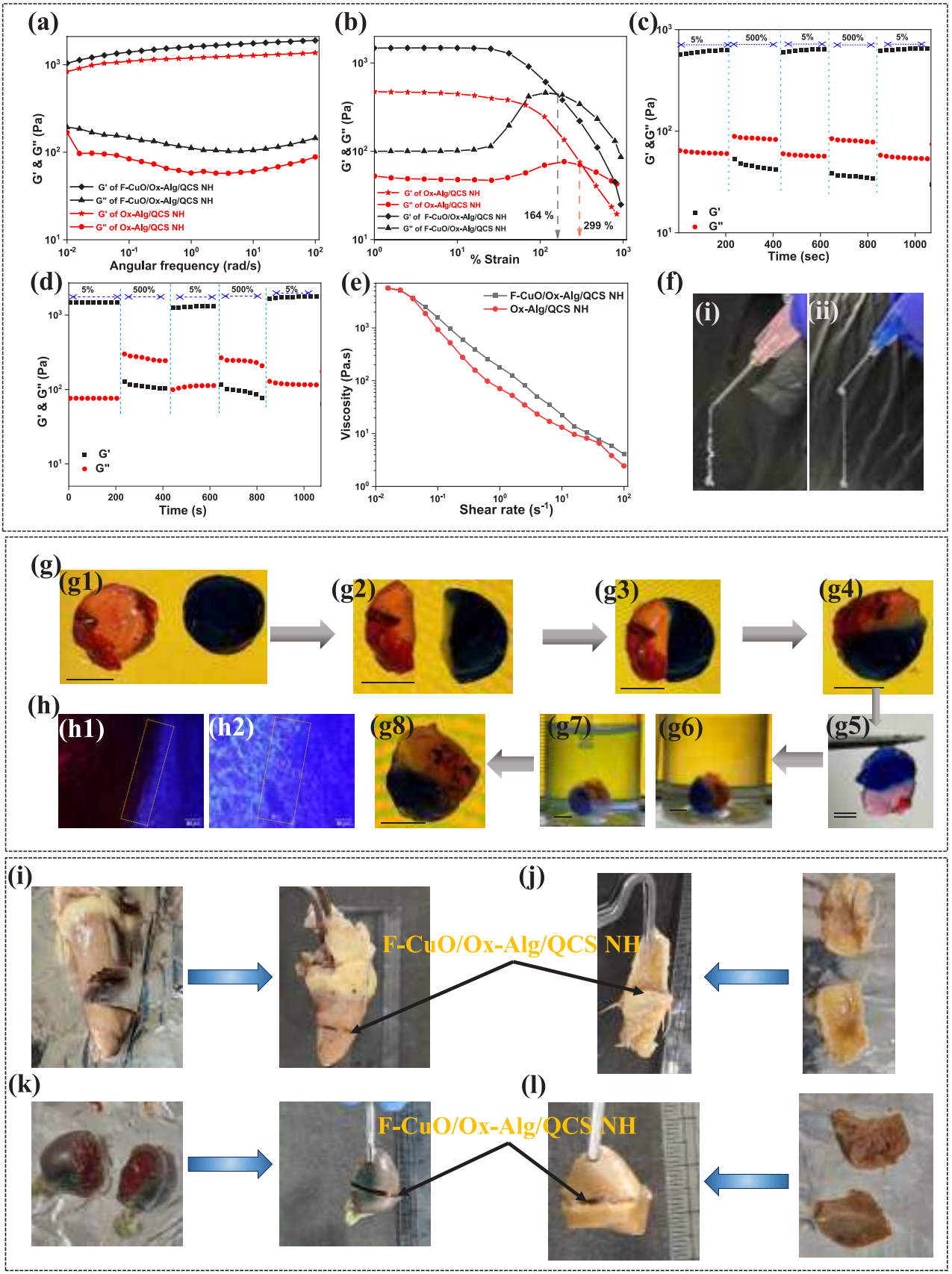

Figure 4. (a-e) Rheological characterization of F-CuO/Ox-Alg/QCS NH and Ox-Alg/QCS NH. (a)) frequency sweep in 0.01 to 100 rad s^{-1} range at a constant strain of 1% at 25°C. (b) stain amplitude sweep in the range of 1 to 800% strain at a constant angular frequency of 10 rad s^{-1} at 25 °C. (c, d) F-CuO/Ox-Alg/QCS NH (c) and Ox-Alg/QC NH (d) are the time scan tests, measured G' and G'' of the hydrogel as a function of time with an alternating strain of 5% and 500% with a constant angular frequency of 10 rad s^{-1} for 200 s at 25 °C. (e) Thixotropic flow sweep test with

https://doi.org/10.1021/acs.biomac.4c00016
Biomacromolecules 2024, 25, 4762−4779

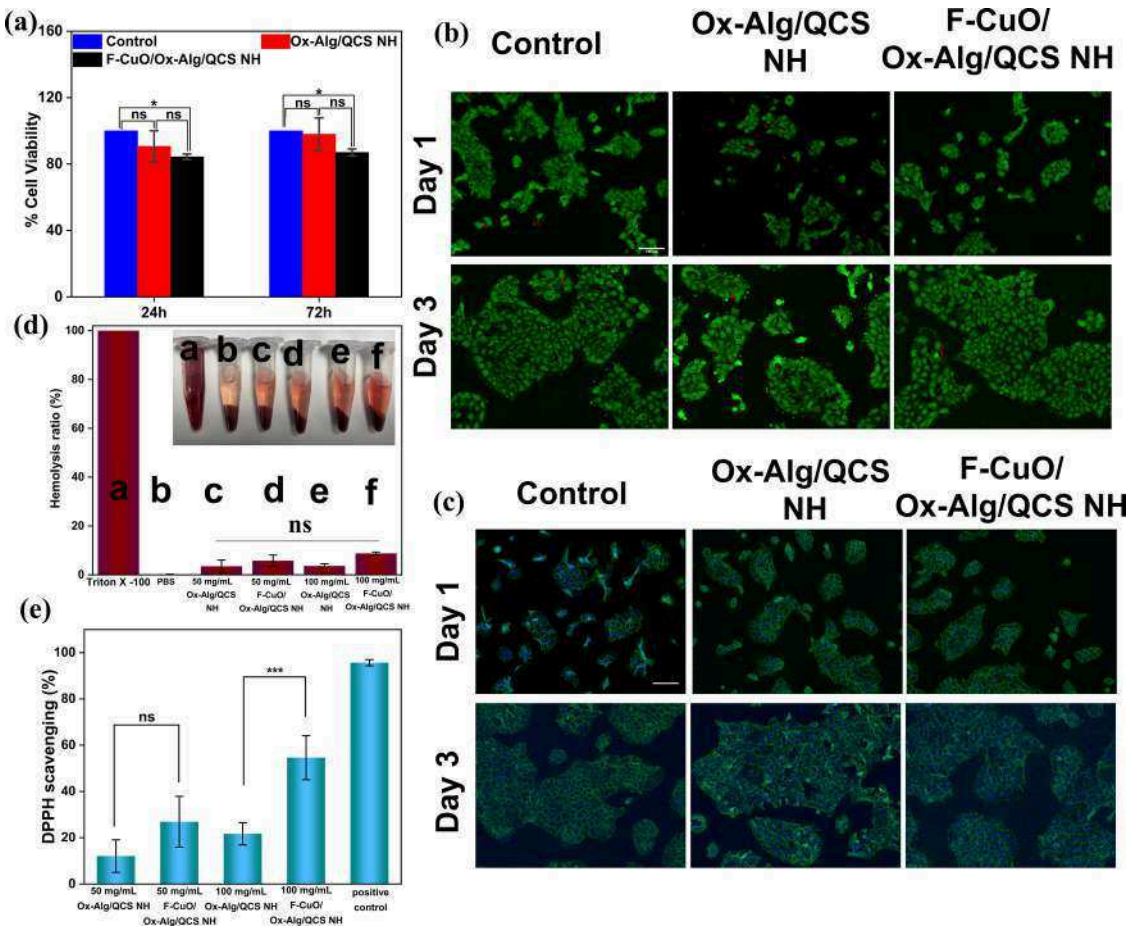

Figure 5. Cytocompatibility of F-CuO/Ox-Alg/QCS NH and Ox-Alg/QCS NH assessed with HaCaT keratinocytes (a) Plot of MTT viability assay of cells exposed to conditioned medium. (b) Fluorescent images of live−dead assay (c)Fluorescence images revealing F-actin (green) and nuclear (blue) organization. (magnification 10 ×, scale bar = 100 μm for all images of (b) and (c)). Control refers to fresh complete culture medium. (d) Hemolytic evaluation of F-CuO/Ox-Alg/QCS NH and Ox-Alg/QCS NH and representative optical photographs of the hemolysis test. (e) DPPH scavenging percentage by F-CuO/Ox-Alg/QCS NH and Ox-Alg/QCS NH with different concentrations and L-ascorbic acid as positive control. Ordinary 2-way ANOVA with Sidak's multiple comparisons test was performed for (a). Ordinary one-way ANOVA with Tukey's multiple comparisons test was performed for (d) and (e). * indicates $p < 0.05$, *** indicates $p < 0.001$, and ns indicates statistically nonsignificant.

gel−sol transition behavior of both the hydrogels was found to be reversible in nature, and interestingly, when the applied oscillatory strain was reduced from 500% to 5%, the system quickly recovered from the quasi-liquid sol to the gel state (Figure 4(c, d). Under 500% strain, hydrogel systems continued in a quasi-liquid state, and upon returning the strain to 5%, both G' and G'' recovered fully without any delay or fatigue. This procedure was similar for both gels and could be performed over many repetition cycles.

A shear rate sweep with a shear rate variation from 0.1 to 100 s^{-1} was investigated to gain more insight into the shear-thinning behavior of hydrogels (Figure 4e). As the shear rate increased, the viscosity of the hydrogels rapidly decreased, and hydrogels showed non-Newtonian shear thinning behavior (Figure 4e). These outcomes validate that both hydrogels have favorable shear-thinning properties for injecting through a needle and syringe for potential administration in a minimally invasive form, which was demonstrated by injecting the hydrogels through 20- and 22-gauge needles. (Figure 4f). These findings suggest that the nanocomposite hydrogel possesses good thixotropic and shear-thinning characteristics and holds potential for use as an injectable soft material.[8]

3.7. Self-Healing Performance of the Hydrogel. The self-healing property is beneficial for hydrogel to recover the damage after its implantation. It is also beneficial for preventing the spontaneous outflow of loaded drugs or particles at nontargeted sites.[58] Any mechanical damage during use can heal to restore its barrier function. A macroscopic self-healing test was performed to assess the self-healing ability of the hydrogels. Each of the two hydrogels with red (stained with rhodamine B) or blue (stained with methylene blue) colors (Figure 4 g1) were cut into two parts using a surgical blade (Figure 4 g2). The two cut pieces of alternating colors hydrogels were placed adjacent to each other (Figure 4 g3) at room temperature. After 3 h, the color of the gel at the edge of the joining became indistinguishable as the two pieces of the hydrogel fused, suggesting that they supported each other without any external aid (Figure 4 (g4, g5)). The proficiency of the two gel pieces to yield a single entity demonstrated the self-healing performance of the F-CuO/Ox-Alg/QCS NH. Furthermore, the stability of the self-healed hydrogel pieces was confirmed by their integrity up to 24 h in PBS (pH 7.4) (Figure 4 (g6, g7)). Additionally, the closer of the gap between the two gel fragments posthealing corroborated with the self-

https://doi.org/10.1021/acs.biomac.4c00016
Biomacromolecules 2024, 25, 4762−4779

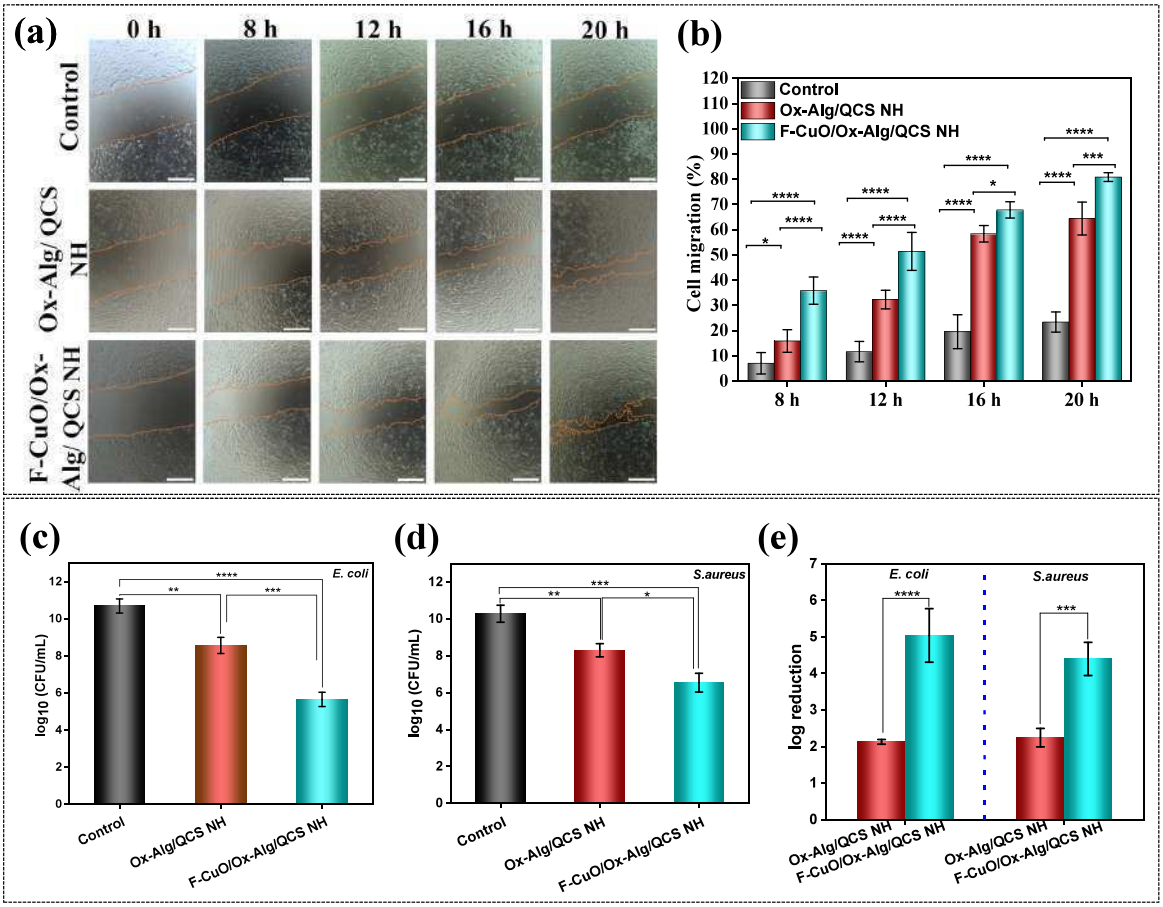

Figure 6. (a) Micrographs of in vitro wound closure. The scale bar of all images is 200 μm. (b) Wound closure rate of endothelial cells when treated with conditioned media of Ox-Alg/QCS NH and F-CuO/Ox-Alg/QCS NH. Control refers to fresh complete culture medium. Ordinary 2-way ANOVA with Tukey's multiple comparisons test was performed for b. (c-e) Antibacterial efficacy of F-CuO/Ox-Alg/QCS NH against (c) Gram-negative *E. coli* and (d) Gram-positive *S. aureus*. (e) log reduction of both hydrogels compared to control against both Gram-positive and Gram-negative bacteria. Ordinary one-way ANOVA with Tukey's multiple comparisons test was performed for (c) and (d). Ordinary 2-way ANOVA with Sidak's multiple comparisons test was performed for (e). **** indicates $p < 0.0001$, *** indicates $p < 0.001$, ** indicates $p < 0.01$, * indicates $p < 0.05$ and ns indicates statistically nonsignificant.

healing capability of the F-CuO/Ox-Alg/QCS NH system as observed in optical micrographs (Figure 4h1, 4h2)).

3.8. Adhesive Properties of the Hydrogel. Since injuries are typically accompanied by bleeding, the adhesive properties of hydrogels in a moist environment are crucial for their application in the biomedical field.[59,60] F-CuO/Ox-Alg/QCS NH system exhibited good potential adhesion to multiple organs, as shown in Figure 4 (i-l). Herein, the adhesive strength was measured by lap-shear tests (Figure S8, SI), and the lap-shear strength of the F-CuO/Ox-Alg/QCS NH is ≈2.56 kPa. The adhesion strength was attributed to the multi-interactions such as ionic interactions, hydrogen bonding due to the hydroxyl group of QCS and Ox-Alg, free-CHO group of Ox-Alg, and amine and quaternized ammonium group of modified chitosan with various proteins of the tissue. Therefore, this hydrogel system could find utility as an adhesive hydrogel in wound dressing, surgical sealants, and other related biomedical applications.

3.9. Cytocompatibility of the Hydrogels. A critical consideration for the effective functioning of a hydrogel as a delivery vehicle and for tissue engineering applications is cytocompatibility.[61,62] The cytocompatibility of both hydrogels was studied with HaCaT keratinocytes. In the actual use of the hydrogel, it would be in direct contact with the skin keratinocytes and fibroblasts at the wound site. Hence, we rationally chose HaCaT cell lines to demonstrate the cytotoxicity of our materials. MTT assay was performed to quantitively assess cell viability by exposing cells to conditioned media containing both degraded and leached products of the gels (Figure 5a). Fresh medium served as the control. More than 80% of the cells were viable over 72 h for both hydrogels, indicating that hydrogels exhibit good cytocompatibility. These results were independently validated by Live/Dead assay, where red represents dead cells and green stained for live cells. Most of the cells were live, with their number increasing over time; however, a very small fraction of dead cells was also observed (Figure 5b). The F-actin and nuclei were stained to observe the morphology of the cells (Figure 5c). Similar cell morphology was observed in conditioned medium-treated cells as well as control groups, and the cells were healthy. Taken together, both hydrogels are cytocompatible.

3.10. Hemolysis Induced by the Hydrogels. In recent years, researchers have made efforts to design novel injectable hydrogels with outstanding blood compatibility, another critical consideration for their in vivo use. The blood compatibility of both the hydrogels at different wet weight concentrations (50 and 100 mg/mL) was assessed *in vitro* via a

https://doi.org/10.1021/acs.biomac.4c00016
Biomacromolecules 2024, 25, 4762−4779

Scheme 2. Schematic Illustration of the Application of Injectable F-CuO/Ox-Alg/QCS Hydrogel with Antibacterial and Antioxidant Properties to Promote Tissue Remodeling

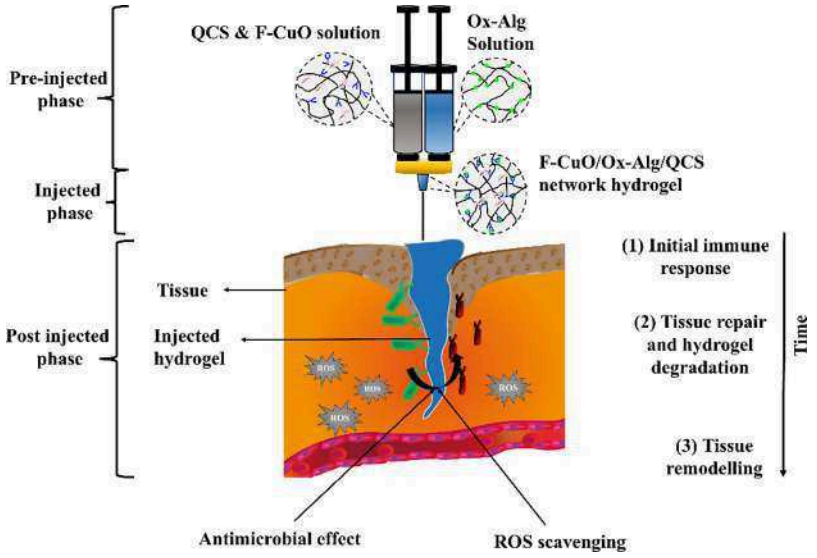

4. DISCUSSION

There are several clinical needs that can benefit from self-healing hydrogels, which have thus received increasing interest in the biomaterials community. Specifically, hydrogels with multifunctional properties are in much demand to develop a multipronged strategy to address the need for effective treatments. Among various needs, chronic wounds affect millions worldwide. The treatment of wounds, internal or external, is a critical clinical challenge, particularly in diabetic and immunocompromised patients. Typically, hemostasis, inflammation, proliferation, and remodeling phases are involved in wound healing.[75] Microbial infections and ROS are influential factors in the wound healing process that can delay each healing phase, resulting in functionally and structurally inadequate results.[76]

Localized administration of antimicrobial agents at the exposed wound site is essential to treat chronic, infected wounds. In this study, the F-CuO-embedded injectable hydrogel with quick gelation time was developed and was shown to exhibit broad-spectrum antibacterial activity with pro-wound healing ability *in vitro*. F-CuO/Ox-Alg/QCS NH showed tissue-like rheological properties and excellent self-healing properties, which can prolong the functionality of the hydrogel and support tissue remodeling. The potent antioxidant activity of F-CuO/Ox-Alg/QCS NH can scavenge free radicals from the wound site and accelerate the healing process. Excellent cytocompatibility and blood compatibility of the developed F-CuO/Ox-Alg/QCS NH can facilitate tissue remodeling. Scheme 2 summarizes the potential application of the nanomaterial-embedded multibiofunctional injectable hydrogel to promote wound healing.

Notably, our formulation of the injectable nanocomposite hydrogel laden with bioligand-functionalized nanomaterials offers a distinctive and attractive combination of properties compared to other hydrogels reported in the literature. We compiled key attributes of recently developed injectable hydrogels reported in the literature and key results of this investigation in Table 1. In contrast to the studies reported by our group and others, the advantages of the system developed here are obvious owing to the unique combination of its properties that can be achieved by incorporating a surface-modified bioactive nanofiller. Unlike our previous study, here we have modified chitosan with GTMAC, which resulted in two benefits: (a) increased solubility of the chitosan in neutral pH or water to prepare the hydrogel, and (b) increased antibacterial activity of the hydrogel network due to the positive charge of trimethylammonium of the substituted GTMAC. Furthermore, while we used the double network cross-linking technique by introducing Schiff base cross-linking chemistry (covalent) and Fe^{2+} ionic cross-linking in the earlier work, here we proposed a novel surface engineering strategy of nanomaterials with a bioligand that can participate in our cross-linking system with the prepolymer of the hydrogel system. Our results indicate that the modification of nanomaterials with the bioligand decreased the cytotoxicity. Most importantly, modifying nanomaterials with bioligands and our cross-linking engineering of hydrogel formation synergistically increase the dispersion of the nanomaterials in the prepolymer solution, and the hydrogel than unmodified nanomaterials (i.e., conventional physical loading). Consequently, the resultant nanocomposite exhibited synergistic benefits of the modified chitosan and CuO-based nanomaterials on cell response for wound healing and antibacterial activity. It is to be noted that the surface modification strategy demonstrated herein is not limited to CuO and can be adapted for other metal/metal oxide nanofillers to generate a library of nanocomposites with tailored attributes for a wide spectrum of biomedical applications. The findings of this work establish a promising multifunctional biomaterial formulation that will require further validation in animal models to establish the biomedical efficacy toward developing potent treatments for specific clinical needs.

5. CONCLUSION

In this work, we proposed a generalized easy approach for surface modification of nanomaterials with a bioligand and developed a degradable polysaccharide-based injectable hydrogel that is shown to be multifunctional, including self-healing, flexible, and antibacterial for biomedical applications. Specifically, bioligand-modified CuO nanosheets were employed to

https://doi.org/10.1021/acs.biomac.4c00016
Biomacromolecules 2024, 25, 4762−4779

Brief of specific publications 2

Chemical Engineering Journal 496 (2024) 153883

Contents lists available at ScienceDirect

Chemical Engineering Journal

journal homepage: www.elsevier.com/locate/cej

"All-in-one" ink for light-based 4D printing of conducting, tough, anti-freezing, and cytocompatible hydrogels

Pritiranjan Mondal, Arkodip Mandal [1], Kaushik Chatterjee [*]

Department of Materials Engineering, Indian Institute of Science, Bengaluru, Karnataka 560012, India

ARTICLE INFO

Keywords:
Conducting hydrogel
4D Printing
Anti-freezing
Dehydration tolerance
Biocompatible

ABSTRACT

High-performance hydrogel-based electronic devices require conducting hydrogels. Conducting hydrogels that are stretchable, soft, and biocompatible are in much demand to fabricate human–machine interfaces, wearable devices, soft robotics, and many other applications. We present a new generation polymeric formulation to prepare hydrogels by digital light processing (DLP)-based three-dimensional (3D) printing technology with visible light that are anti-freezing, electrically conductive, tough, stretchable, and non-toxic. The printed conducting hydrogels have exceptional water-holding capability at atmospheric conditions and tolerance to freezing over a wide range of temperatures from − 80 to 45 °C. The inks are amenable to the manufacturing of four-dimensional (4D)-printed hydrogels that can elicit pre-programmed structural deformations. This work presents polymeric formulations for potentially designing ultrafast programmable electronic devices with printed hydrogel electronics in various biomedical applications, soft robotics, biosensors, flexible electronics, human–machine interfaces, and health monitors for use under extreme environmental conditions.

1. Introduction

Recently, conducting hydrogels have attracted much interest in the biomedical and biomaterials community to combine flexible and stretchable hydrated polymer structures with intriguing electronic functionalities [1,2]. These multifunctional materials combining the hydrogel characteristics along with the conductive components, such as electrical conductivity and electrochemical-redox properties, open new opportunities in the biomedical field, such as biosensors [3], soft robotics [4], flexible electronic devices [5], drug delivery [6], tissue engineering [7], health monitors [8]. However, conventional preparation techniques such as transfer printing and photolithography are limited to producing simple structural devices [9]. Several constraints of conventional manufacturing tools are increasingly being circumvented by three-dimensional (3D) printing techniques [10–12]. Although there is a limited library of conducting hydrogels reported in the literature, most are not amenable to 3D printing. Digital light processing (DLP)–based 3D printing yields parts of complex design architecture with high accuracy and fidelity necessary to develop and create complex structures [13].

A key limitation of conventional hydrogels is their limited working conditions, such as poor durability for use over extended periods or use in extreme conditions other than ambient conditions, such as low temperatures [14,15]. Once the temperature falls below the freezing point of water, conventional hydrogels have a strong tendency to freeze. The frozen hydrogels lose their original functionality, including elasticity and conductivity, in the case of a few reported conductive hydrogel formulations, which significantly restricts their practical use in cold environments (such as high altitudes or seasonally low temperatures) [16,17]. Moreover, typical hydrogels dehydrate rapidly, even at ambient conditions, leading to hardness, distortion, and failure to preserve desirable properties over time. Researchers have developed organohydrogels that combine an organic solvent with the polymeric network to overcome these challenges [18,19]. However, organohydrogels typically have poor conductivity at low temperatures, are difficult to polymerize, and are not compatible with DLP-based 3D printing. Organohydrogels are not sufficiently cytocompatible for implantable biomedical applications. Novel polymer formulations based on poly(3,4-ethylenedioxythiophene) (PEDOT), which augments the processability of PEDOT through 3D printing techniques, have been investigated [20,21]. Recently, it has been demonstrated that PEDOT can undergo copolymerization with various bio-polyesters, such as poly

* Corresponding author.
E-mail address: kchatterjee@iisc.ac.in (K. Chatterjee).
[1] Current Address: Department of Chemical and Biological Engineering, University of Colorado Boulder, Boulder, CO 80303, USA.

https://doi.org/10.1016/j.cej.2024.153883
Received 25 April 2024; Received in revised form 21 June 2024; Accepted 8 July 2024
Available online 9 July 2024

(lactic acid) (PLA) and poly(ε-caprolactone) (PCL), resulting in graft copolymers [22,23]. These copolymers exhibit shear-thinning behavior, making them amenable to direct ink writing (DIW) and show good cytocompatibility. However, these modifications decrease the conductivity and functionality of PEDOT. Therefore, designing multifunctional hydrogels that can withstand freezing and dehydration while maintaining desired mechanical performance, good conductivity, and cytocompatibility, as well as being amenable to additive manufacturing, is a key challenge.

The goal of this study was to design a photocurable and conductive polymer ink based on poly(3,4-ethylenedioxythiophene) polystyrene sulfonate (PEDOT:PSS) intended for processing via DLP-based 3D printing to yield multifunctional hydrogels that can overcome the limitations associated with the current generation of hydrogels. The ink formulations were rationally developed with PEDOT:PSS, acrylamide, synthesized crosslinker pluronic F-127 dimethacrylate (PF127DMA), and LiCl as an anti-freezing agent to impart different properties. The ink was systematically developed based on the processability and

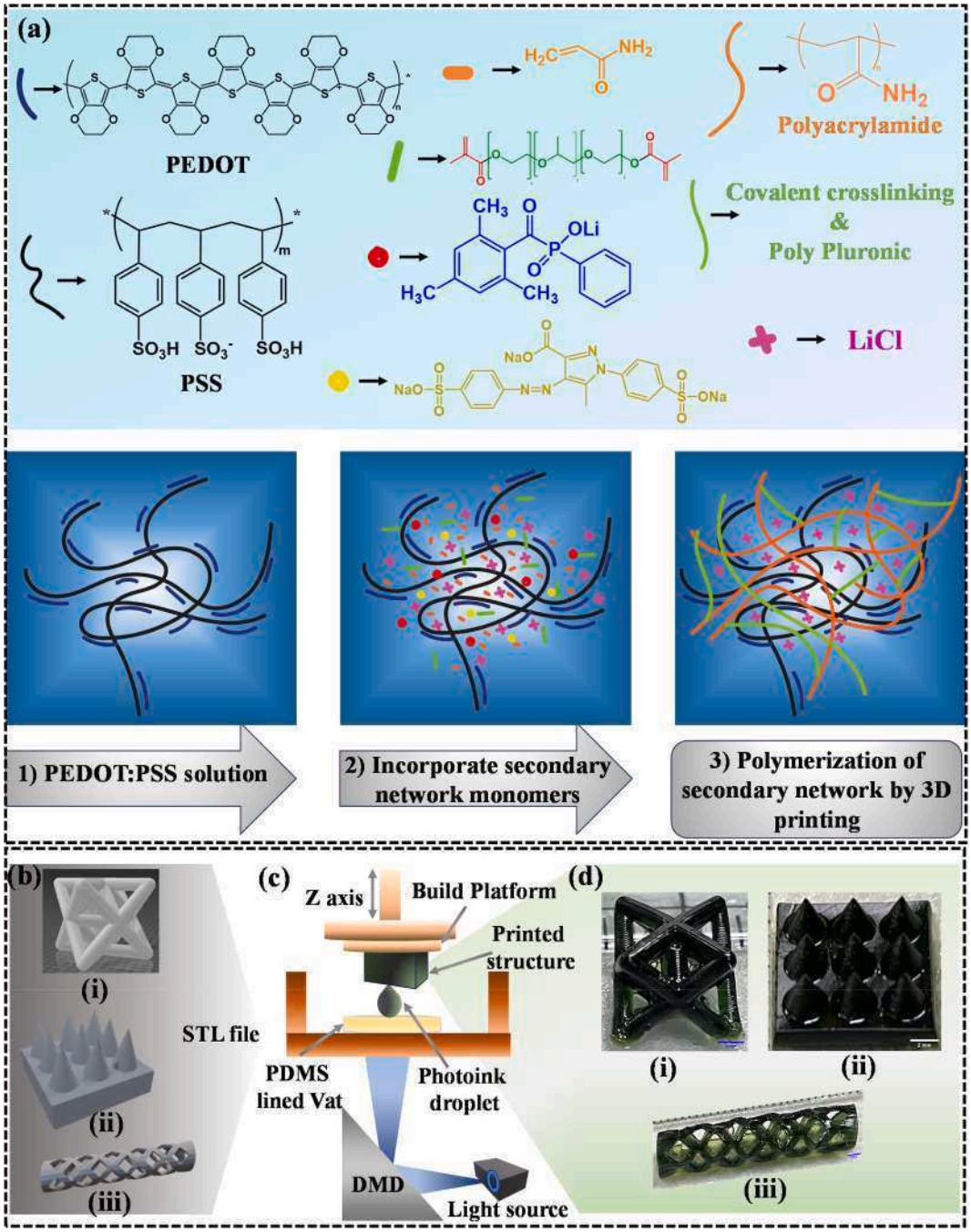

Fig. 1. Ink composition and fabrication process to prepare conducting interpenetrating network hydrogels. (a) Scheme for formulating an ink for fabricating conducting hydrogels. First, aqueous solutions of PEDOT: PSS were prepared using DMSO and glycerol to screen the electrostatic repulsions between PEDOT and PSS. Next, the PEDOT: PSS solution was infiltrated with acrylamide, PF127DMA, LiCl, Tartrazine, and LAP. Finally, the polyacrylamide network crosslinked with PF127DMA plus poly pluronic was formed by polymerizing the monomers via DLP-based 3D printing technique; (b) STL file of different parts of complex geometry (i) octet-truss, (ii) fine needles, and (iii) a biostent; (c) Scheme demonstrating layer-by-layer fabrication by blue light (405 nm) using a DLP-based 3D printer; (d) digital photographs of the 3D-printed parts corresponding to the STL files in (b) (scale bar is 2 mm). (For interpretation of the references to colour in this figure legend, the reader is referred to the web version of this article.)

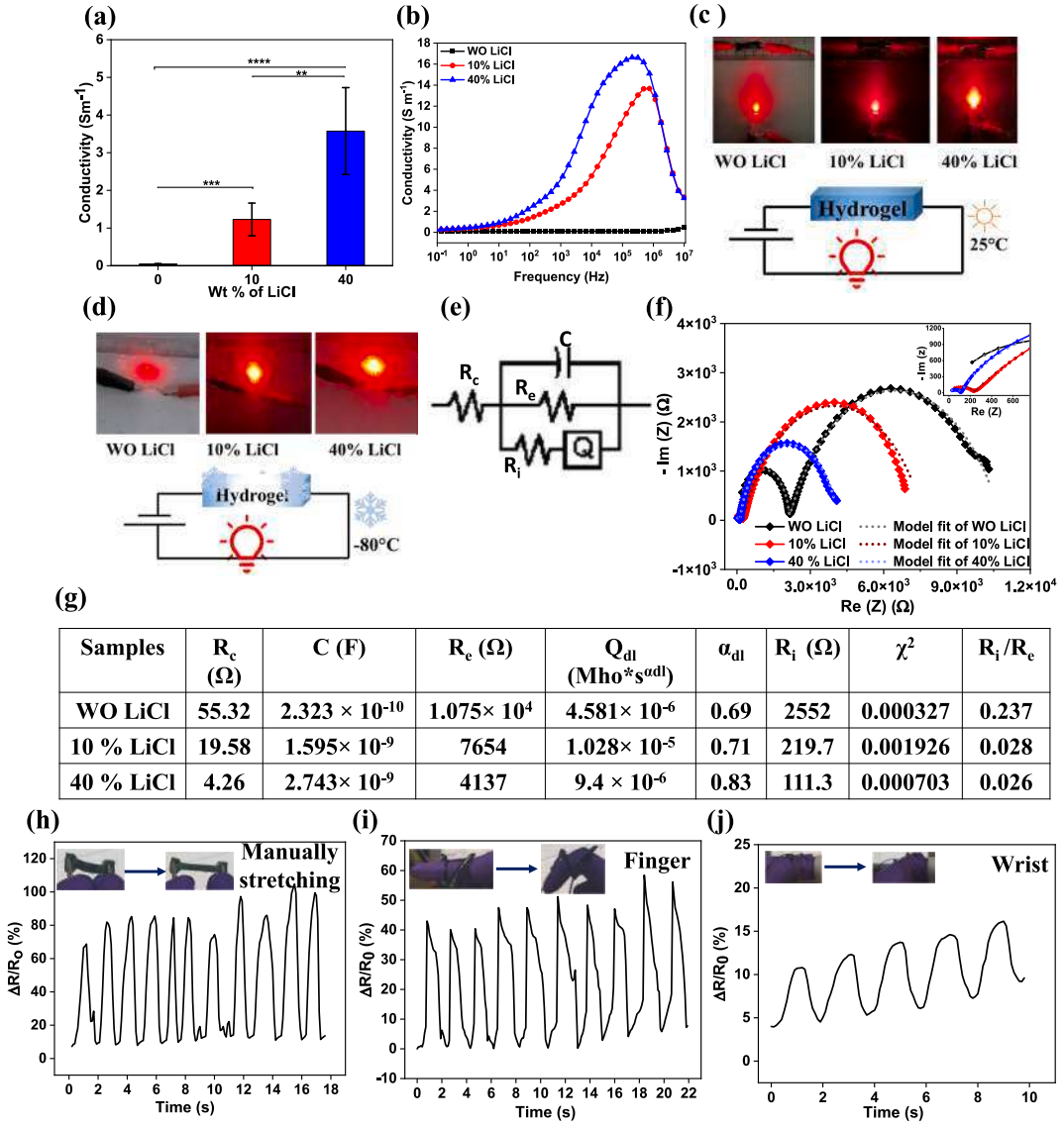

Samples	R_c (Ω)	C (F)	R_e (Ω)	Q_{dl} (Mho*$s^{\alpha dl}$)	α_{dl}	R_i (Ω)	χ^2	R_i/R_e
WO LiCl	55.32	2.323×10^{-10}	1.075×10^{4}	4.581×10^{-6}	0.69	2552	0.000327	0.237
10 % LiCl	19.58	1.595×10^{-9}	7654	1.028×10^{-5}	0.71	219.7	0.001926	0.028
40 % LiCl	4.26	2.743×10^{-9}	4137	9.4×10^{-6}	0.83	111.3	0.000703	0.026

Fig. 5. Conductivity and electrochemical characterization of WO LiCl, 10 % LiCl, and 40 % LiCl 3D-printed hydrogels: (a) Conductivity values of the 3D-printed hydrogel structures were calculated by measuring resistance using a standard four-point probe head. Data are plotted as mean ± S.D. for n = 3. Ordinary one-way ANOVA with Tukey's multiple comparisons test was performed for (a). ** indicates $p < 0.01$, *** indicates $p < 0.001$, **** $p < 0.0001$. (b) AC electrical conductivity of the hydrogels as a function of frequency. Demonstration of the printed hydrogels functioning as conductors at (c) 25 °C and (d) − 80 °C. (e) Equivalent circuit model representation for fitting the electrochemical impedance spectroscopy (EIS) curve of the hydrogels. R_c, R_e, and R_i represent the solution resistance, charge transfer resistance, and ionic resistance, respectively. C represents the double-layer capacitance. Q represents the constant phase element (CPE), which is used to account for inhomogeneous or imperfect capacitance, and is represented by the parameters Q and α, where Q is the capacitance impedance value and α represents the deviation from ideal capacitive behavior. The true capacitance (C) can be calculated from these parameters by the relationship $C = Q\,\omega_{max}^{\alpha-1}$, where ω_{max} represents the frequency at which the imaginary component reaches a maximum (f) Nyquist plot obtained from performing electrochemical impedance spectroscopy through the hydrogel, overlaid with the plot predicted from the equivalent circuit model (mentioned in (e)). Impedance was measured between 0.1 Hz and 10^6 Hz. (g) Values for all relevant parameters were extracted for the three hydrogel formulations by fitting their EIS data with the equivalent circuit model. (h, i, j) Real-time sensing performance of the 40 % LiCl hydrogel as strain sensor in monitoring human activities. (h) Dynamic response to strain under repeated manual stretching of the hydrogel, and variation of resistance during human activities of (i) finger bending, and (j) wrist bending.

designer 3D-printed hydrogels presented here.

Electrochemical impedance spectroscopy (EIS) also serves as a responsive indicator for a broad spectrum of physical and chemical properties. There is currently a discernible trend toward the proliferation of impedimetric biosensors. The techniques of impedimetric analysis have been employed to distinguish the development of biosensors and to scrutinize the catalytic reactions of enzymes, nucleic acids, lectins, receptors, whole cells, antibodies, etc. Therefore, for bio-interfacing applications, it is essential to characterize the impedance of the hydrogel as the presence of ions in bodily fluids can additionally contribute to the conductivity of the printed hydrogel electrodes, particularly given the high liquid content of the hydrogels. To decouple ionic and electronic conductivities, we saturated the printed hydrogels in 1 M phosphate-buffered saline (PBS) solution and characterized their impedance using electrochemical impedance spectroscopy (EIS) in PBS as an electrolyte. The intercept of these EIS curves with the real axis is taken as the impedance of hydrogels. The data were fitted to the equivalent circuit model illustrated in Fig. 5e, where R_e, R_c, and R_i represent the electronic resistance, charge transfer resistance, and ionic resistance of the cell assembly, respectively. Q and C represent the constant phase elements and capacitance arising from ionic conduction and double layer formation of the hydrogel, respectively. The two

distorted semicircular shapes of the Nyquist plot suggest the presence of comparable ionic and electronic conductivities (refer Fig. 5f and the inset). The parameters extracted from fitting the data to the equivalent circuit model confirm that the ionic and electronic resistances decreased with an increase in LiCl content in the hydrogel (refer Fig. 5g). In the WO LiCl hydrogel, R_e is 1.075×10^4 Ω, and R_i is 2552 Ω, which decreases one order in the presence of LiCl. R_i sharply decreased to 219.7 Ω and 111.3 Ω for 10 % LiCl and 40 % LiCl, respectively. This demonstrates that the relative contribution of electronic conductivity to the overall impedance of the hydrogel decreases with the increase of the ionic component, Li^+ & Cl^- in the hydrogel system (refer Fig. 5g). However, both resistances decrease due to the presence of LiCl in the hydrogel system. The improvement of this conductivity can be attributed to the following two effects. One contribution is that of Li^+ ions in the double network polymer hydrogel, and the other is the π electron conjugated polymer of PEDOT [2]. As the LiCl content increased, more free electrons and ions led to more effective ion transport paths and enhanced ion diffusion kinetics.

2.7. Application of the hydrogel for human bodily motion detection

The developed hydrogel demonstrates significant potential as a sensor for monitoring both large-scale and minute human movements due to its excellent electrical conductivity and stretchability. To demonstrate this potential, we evaluated the sensing performance of a 40 % LiCl hydrogel by measuring the changes in relative resistance with

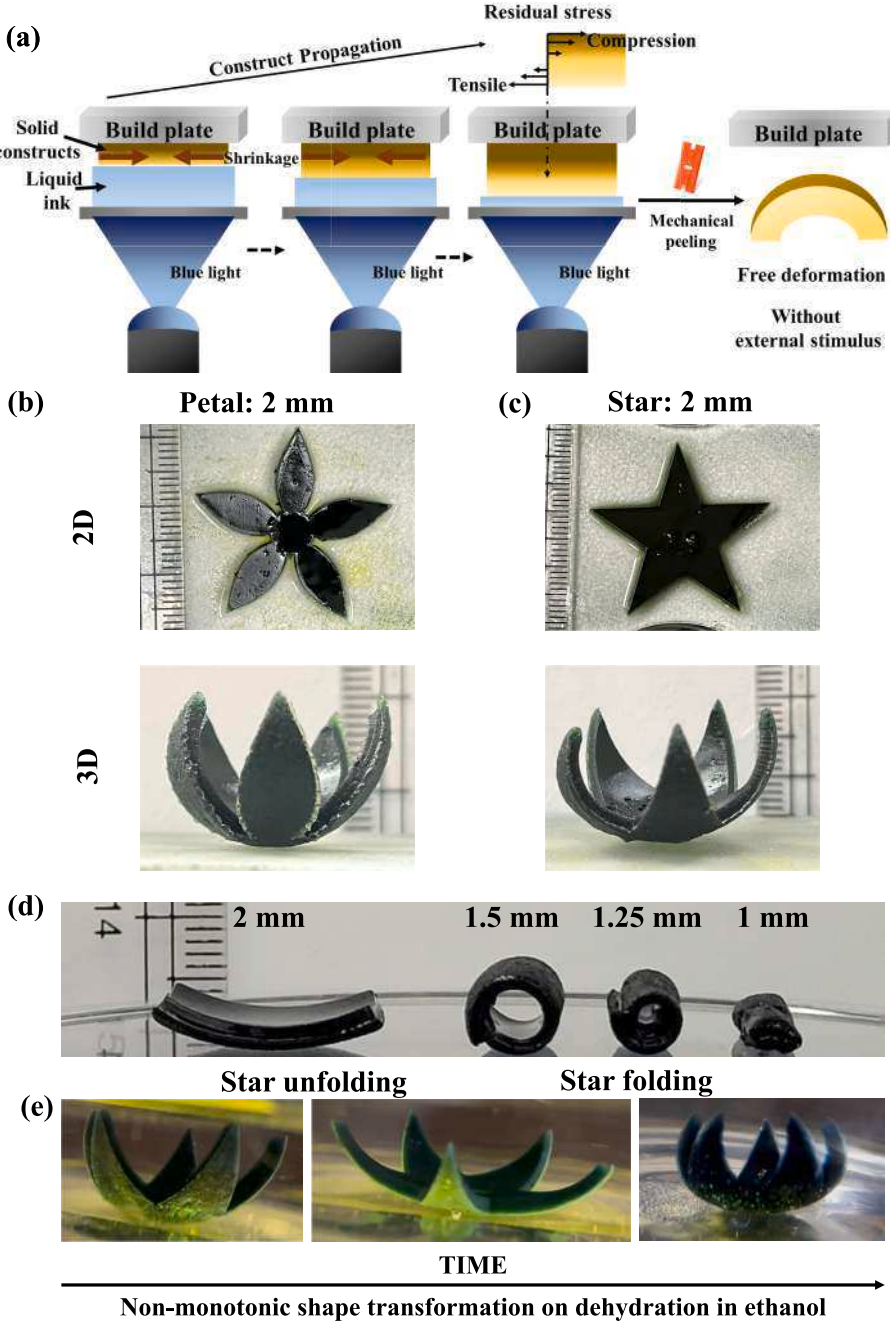

Fig. 6. (a) Schematic illustration depicting the free-form deformation of DLP-printed hydrogel on peeling. The 2D to 3D transformation of (b) a petal structure (c) a star structure on mechanical peeling. (d) The degree of curvature of a flat sheet is dependent on the thickness of the printed sheet, with the curvature decreasing with increasing thickness. (e) Non-monotonic shape changes exhibited by these hydrogels (unfolding and then folding again) on dehydration in alcohol.

time during stretching of the hydrogel. The strain sensor exhibited sharp and rapid real-time changes in resistance in response to manual stretching of the hydrogel (Fig. 5h, Video V1) and large limb motions, including finger bends (Fig. 5i, Video V2) and wrist bends (Fig. 5j, Video V3). These results demonstrate that the 40 % LiCl hydrogel-based sensors can be further developed and engineered for adoption in motion monitoring as strain sensors. Notably, the amplitude of finger and wrist bends can be distinctly identified by the width of the signal peak (Fig. 5 (i, j)). Furthermore, the signals for the same motion were very consistent, indicating the high sensitivity and superior recoverability of the hydrogel. The excellent sensing performance of the hydrogel suggests its capability to monitor motion in real time and avoid mechanical damage caused by stretching. Therefore, the hydrogel can be projected to serve as a stretch-assisted, safe, and precise strain sensor in various fields of application.

2.8. Shape-morphing parts: 4D printing

Whereas 3D printing of the ink has already been demonstrated to yield additively manufactured hydrogels of complex and intricate architectures, we next explored the ability to transform DLP-printed constructs in a programmable manner without cumbersome stimulation into shapes that may not be realizable through conventional 3D printing. This facile transformation of the 4D-printed structure is realized through the free deformation of the DLP-printed construct through mechanical peeling off the build plate (refer Fig. 6). The free deformation of the DLP-printed construct occurs spontaneously under the influence of the internal residual stresses that are generated from the layer-by-layer 3D printing process, obviating the need for an external stimulus (moisture, temperature, humidity, light, or electric/magnetic fields). The transformed structure post-DLP-printing retains its altered configuration even in aqueous environments, underscoring the method's simplicity in conferring a permanent transformation to the DLP-printed construct. Additionally, owing to the interplay of geometry and stress effects [27], the transformed construct exhibits far-from-equilibrium shape changes in ethanol. This unique characteristic can be strategically exploited to design dynamic constructs with diverse applications in the biomedical field.

The mechanism of the free-form deformation through mechanical peeling has been elucidated by Zhao et al. [28], albeit not in the context of DLP-based 3D printing. The photopolymerization of the hydrogel precursor is accompanied by volume shrinkage due to covalent bond formation between the monomers (acrylamide) and the crosslinkers (PF127DMA) and is more pronounced at higher crosslinking densities [29]. During the sequential layer-by-layer printing process, a non-uniform stress gradient is generated, as described in an earlier study [30]. However, since the construct is physically constrained to the build, no deformation is observed at this stage. At the end of the printing process, the last cured layer experiences tensile residual stresses, and the first cured layer experiences compressive residual stresses. When peeled, the physical constraints preventing any shape change are removed, and the construct undergoes free-form deformation (refer Fig. 6a). The tensile residual stresses result in contraction, while the compressive residual stresses result in expansion. This results in the construct bending with the last cured layer as the concave side (refer Fig. 6 (b, c)). It is important to note that the shrinkage-induced deformation is prominent at higher crosslinker concentrations (16 wt%) and essentially vanishes at lower crosslinker concentrations (4 wt%) when the volume shrinkage is less. At higher thicknesses, the bending stiffness increases, which makes it difficult to bend the rectangular beam. While the shrinkage-induced bending phenomenon is pronounced at a thickness of 1 mm with the beam curling onto itself from both ends, the bending is significantly less pronounced at thicknesses beyond 2 mm (refer Fig. 6 d). Thus, the thickness of the printed construct can be tuned to obtain the desired degree of deformation.

Owing to mechanical programming, the curved shape presents a non-uniform stress state. The outer surface is in a state of tension, while the inner surface is in a state of compression. The diffusivity of water molecules into the hydrogel is strongly correlated with the stress state. Specifically, the water diffusivity can be expressed as $D = D_o e^{\sigma_h \frac{\Omega}{k_B T}}$, where D_0 signifies the diffusivity under conditions of zero stress, σ_h denotes the hydrostatic stress derived from the trace of the stress tensor, Ω represents the activation volume governing water diffusion, and k_BT corresponds to the thermal energy. Regions experiencing a state of tension (positive σ_h) exhibit higher water diffusivity, while regions experiencing a state of compression exhibit slower water diffusivity. The geometry plays a minor synergistic effect, with the outer surface experiencing faster diffusion due to the larger surface area. When the swollen hydrogels are placed in ethanol, they undergo dehydration, with the outer surface losing its water content faster than the inner surface due to faster diffusion as a consequence of both stress and geometry effects. This temporal difference in swelling kinetics causes the non-monotonic far-from-equilibrium shape-morphing behavior [27], which leads to the opening of the hydrogel structures as the outer surface experiences faster water loss and shrinks faster compared to the inner surface (refer Fig. 6e, Video V4, Video V5). As a result, the outer surface reaches equilibrium earlier than the inner surface. Next, the construct returns to its initial shape as the inner surface reaches equilibrium (refer Fig. 6e, Video V4, Video V5). The ability to program (through peeling) and re-program the hydrogels (through dehydration in ethanol) is unique to this system, and such a phenomenon has not been reported in the literature. The programmability of these hydrogels makes them attractive candidates for applications in flexible electronics, biosensing, drug delivery, and tissue engineering.

2.9. In vitro cytocompatibility of hydrogels

Cytocompatibility is essential for applying the conducting hydrogel for biomedical and biosensor applications, particularly if implanted. We studied the cytocompatibility of the 3D-printed hydrogel constructs against L929 mouse fibroblasts (refer Fig. 7). Cells were seeded and cultured for 36 h, and then the 3D-printed gel was placed in the wells, as shown schematically in Fig. 7a, and cultured further to evaluate the effect on the cells. Alamar blue assay revealed that more $>$ 80 % of cells and $>$ 75 % of cells were viable after exposure to the gels for 1 and 4 days, respectively, for all three hydrogel formulations (refer Fig. 7b). However, on day 4, WO LiCl showed $>$ 90 % cell viability, whereas viability was $\approx$ 80 % and $\approx$ 76 % for 10 % LiCl and 40 % LiCl hydrogels, respectively. Additionally, the Live-Dead assay was performed to independently validate toxicity qualitatively (refer Fig. 7c). It was observed that most cells were alive (green), and the number of cells increased with time, which indicates cells are viable and continue to proliferate in the presence of the 3D-printed gels. However, the number of dead (red) cells increased marginally on day 4 for 40 % LiCl gel. This may be due to the release of Li^+ and Cl^- into the culture media. Furthermore, we also observed the morphology of the cells and compared them with the control groups by staining and imaging F-actin and nuclei (refer Fig. 7d). It was seen that the cell morphology of the sample-treated groups was similar to that of the control group, and no distortion in morphology was observed for WO LiCl and 10 % LiCl gels. However, cells in the presence of the 40 % LiCl gels showed some differences in morphology compared to the control group, which could be the effect of Li^+ and Cl^- ions. Taken together, these results suggest that cells are viable in the presence of the 3D-printed hydrogels developed here and could be explored for biomedical applications. More detailed in vivo investigations are warranted to establish the biocompatibility of the hydrogels for implantable applications.

3. Discussion

This work presents new polymeric ink formulations that are

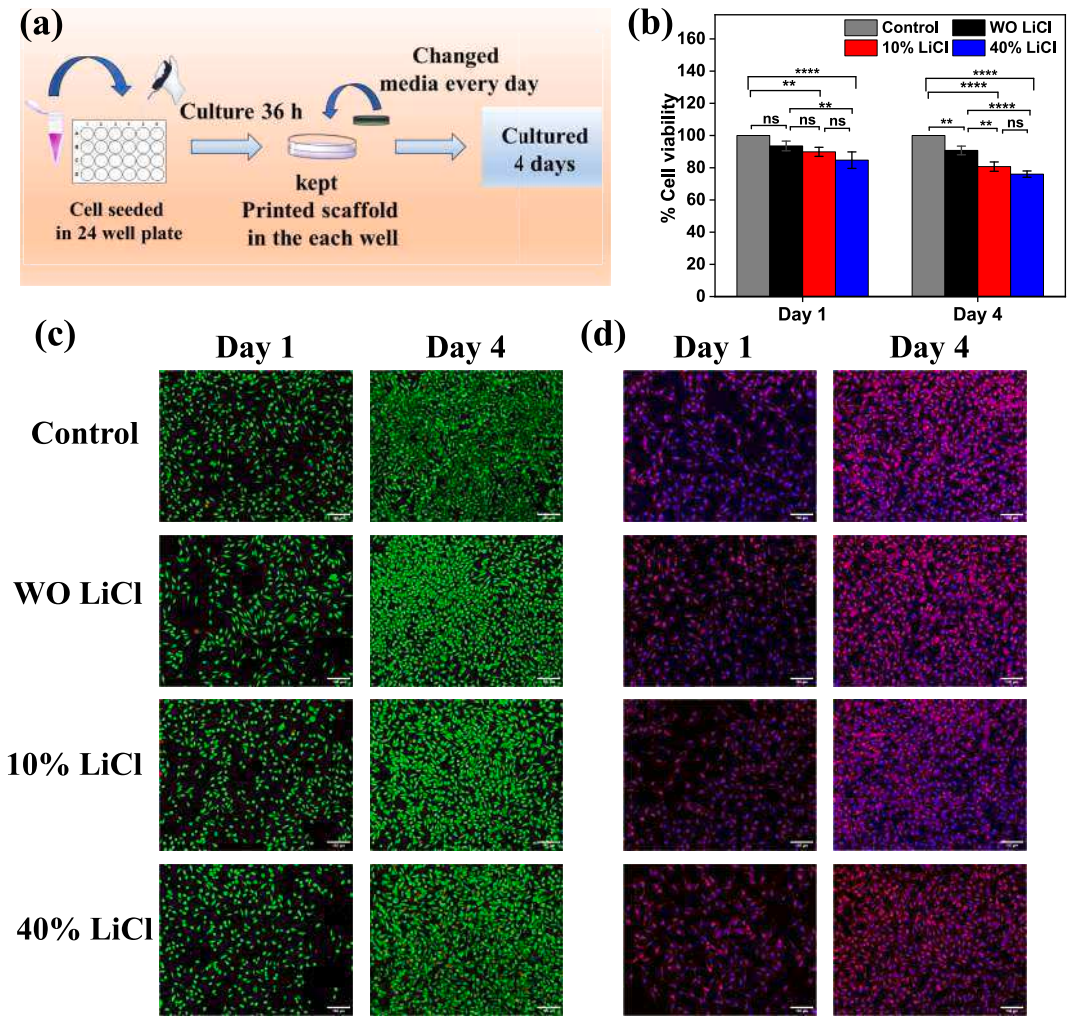

Fig. 7. Cytocompatibility assessment of the 3D-printed hydrogel structures against L929 mouse fibroblasts: (a) Scheme summarizing the experimental approach to evaluate the cytotoxicity of the hydrogels. Cell viability was assessed with respect to the control (cells cultured in fresh medium) by (b) Alamar blue assay, (c) Live (green)- Dead (red) assay, and (d) F-actin (red) and nuclear (blue) imaging to evaluate cell morphology (magnification 10×, scale bar = 100 μm for all images of (c) and (d)). Ordinary 2-way ANOVA with Tukey's multiple comparisons test was performed for (b). ** indicates $p < 0.01$, **** indicates $p < 0.0001$, and ns indicates statistically non-significant. (For interpretation of the references to colour in this figure legend, the reader is referred to the web version of this article.)

compatible with state-of-the-art manufacturing technologies, specifically DLP-based 3D printing, for fabricating highly conductive hydrogels with dual electronic and ionic conductivity and highly tunable mechanical properties. We compiled the salient properties of the recently developed conducting hydrogels described in the literature and the findings of this investigation in Table 1 (qualitative summary) and Table S4, SI (detailed comparison). The unique combination of highly sought properties makes our hydrogels promising candidate materials

Table 1
Comparison of the multifunctional properties of the present study with reports in the literature. ✔ and ✘ denote the presence and absence of the functional properties, respectively.

Study	Additive manufacturing	Anti freezing	Dehydration tolerance	Flexibility	Cytocompatibility	4D deformation	Ref.
Feig et al. (2018)	✘	✘	✘	✘	✘	✘	[2]
Fantino et al. (2018)	✔	✘	✘	✘	✘	✘	[31]
Kaveh et al (2018)	✘	✘	✘	✘	✔	✘	[7]
Jordan et al (2021)	✔	✘	✘	✘	✘	✘	[32]
Ge et al (2021)	✘	✔	✔	✔	✘	✘	[25]
Zhu et al. (2021)	✔	✘	✘	✔	✘	✘	[33]
Zhang et al. (2022)	✔	✘	✘	✔	✘	✘	[1]
Larrea et al. (2022)	✔	✘	✘	✔	✘	✘	[34]
Zhang et al. (2022)	✔	✘	✘	✔	✘	✘	[35]
Cai et al. (2023)	✘	✔	✔	✘	✘	✘	[26]
Cheng et al (2023)	✔	✘	✘	✔	✘	✘	[36]
Chen et al. (2024)	✘	✔	✔	✔	✘	✘	[16]
This Work	✔	✔	✔	✔	✔	✔	

for integration into wearable and implantable devices, for which the ability to couple high electronic conductivity with low modulus to high modulus and high stretchability is particularly attractive and could also fund use in soft robotics and machine-tissue interfaces particularly soft tissues such as the brain, cardiac tissues, and skeletal muscles. In addition, the ability to tune the mechanical properties of our hydrogel without compromising its conductivity makes it an attractive materials platform for various applications in the field of hydrogel-based electronics since it is well known that cells are highly responsive to the mechanical properties of their micro-environment. Our developed conducting hydrogels can provide a pathway for electrical stimulation and recording while maintaining the necessary 3D architecture and offering optimal mechanical properties tailored for each tissue. These conducting hydrogels could also be developed to be seamlessly incorporated into application-specific devices by 3D printing processes, enabling diverse shapes and complex geometries tailored to specific target applications. Importantly, these hydrogels also exhibit freezing- and dehydration-tolerance properties and show excellent flexibility in extremely low temperatures, as low as −80 °C. Therefore, the freezing- and dehydration-tolerant attributes incorporated into our 3D-printed hydrogels render their functionality and durability remarkable for the longer life span of use in terms of stretchability and conductivity concurrently. Another unique attribute of the ink formulation is that it is amenable to 4D printing to yield conducting hydrogels that can also undergo structural deformations in a programmable manner. The 3D-printed gels also show good cytocompatibility. Therefore, these all-in-one ink formulations developed here offer a unique combination of attractive attributes for potential use in diverse applications, including in extremely cold and hot working conditions, unlike the limited working conditions for other hydrogels, and we envisage its role in accelerating advancement in many fields.

4. Conclusion

We have developed photopolymerizable and conductive PEDOT: PSS-based inks and utilized them for additive manufacturing by DLP-based 3D printing to fabricate multifunctional hydrogels. The rapid fabrication process of the 3D printing system involves developing hydrogel by integrating the interpenetrating primary network of PEDOT: PSS and in situ formation of the secondary network of polyacrylamide, which is simultaneously crosslinked with synthesized PF127DMA, which leads to a stable hydrogel network with the desired functionality without additional manufacturing steps. Additional key innovations lie in the multifunctionality of the 3D-printed hydrogels, including tunable mechanical properties, anti-freezing properties, and dehydration tolerance ability through the strong interaction of Li^+ and Cl^- ions with polymer networks. The 3D-printed hydrogels exhibit remarkable mechanical stretchability (% elongation up to 1000 %), superior toughness (~114 kJ m^{-3}), durability (outstanding fatigue resistance, resilience, and cyclic stability), exceptional anti-freezing properties (until −80 °C), and excellent conductivity (≈ 3.57 $S.m^{-1}$) and impedance characteristics. Additionally, the 3D-printed constructs can exhibit programmable 4D deformations. The 3D-printed hydrogels demonstrate favorable cytocompatibility in vitro. Given the attractive combination of attractive properties, these 3D/4D-printed hydrogels are promising candidates for application across diverse domains, particularly bio-electronic applications in healthcare and other fields.

Author contributions

The work was conceived by PM and KC. PM performed all the experiments and analyzed data. AM contributed to 3D and 4D printing. PM prepared the first draft of the manuscript. All authors have edited the manuscript. KC is the senior author overseeing the work.

CRediT authorship contribution statement

Pritiranjan Mondal: Conceptualization, Data curation, Formal analysis, Investigation, Methodology. **Arkodip Mandal:** Writing – review & editing, Investigation, Methodology, Data curation, Formal analysis. **Kaushik Chatterjee:** Conceptualization, Funding acquisition, Project administration, Writing – review & editing, Supervision, Funding acquisition.

Declaration of competing interest

The authors declare that they have no known competing financial interests or personal relationships that could have appeared to influence the work reported in this paper.

Acknowledgments

Support from the Science and Engineering Research Board (SERB) and the Government of India (IPA/2020/000025) is gratefully acknowledged. The authors thank the NMR Centre and MNCF at IISc for access to characterization facilities. The authors thank Prof Suryasarathi Bose at IISc for access to the rheometer.

Appendix A. Supplementary data

Supplementary data to this article can be found online at https://doi.org/10.1016/j.cej.2024.153883.

References

[1] Y. Zhang, L. Chen, M. Xie, Z. Zhan, D. Yang, P. Cheng, H. Duan, Q. Ge, Z. Wang, Ultra-fast programmable human-machine interface enabled by 3D printed degradable conductive hydrogel, Materials Today Physics 27 (2022) 100794, https://doi.org/10.1016/j.mtphys.2022.100794.
[2] V.R. Feig, H. Tran, M. Lee, Z. Bao, Mechanically tunable conductive interpenetrating network hydrogels that mimic the elastic moduli of biological tissue, Nat. Commun. 9 (2018) 5030, https://doi.org/10.1038/s41467-018-07487-1.
[3] D.K. Patel, A.H. Sakhaei, M. Layani, B. Zhang, Q. Ge, S. Magdassi, Highly stretchable and UV curable elastomers for digital light processing based 3D printing, Adv. Mater. 29 (2017) 1606000, https://doi.org/10.1002/adma.201606000.
[4] Y. Zhou, C. Wan, Y. Yang, H. Yang, S. Wang, Z. Dai, K. Ji, H. Jiang, X. Chen, Y. Long, Highly stretchable, elastic, and ionic conductive hydrogel for artificial soft electronics, Adv. Funct. Mater. 29 (2019) 1806220, https://doi.org/10.1002/adfm.201806220.
[5] H. Yang, W.R. Leow, X. Chen, 3D printing of flexible electronic devices, Small Methods 2 (2018) 1700259, https://doi.org/10.1002/smtd.201700259.
[6] M. Bansal, A. Dravid, Z. Aqrawe, J. Montgomery, Z. Wu, D. Svirskis, Conducting polymer hydrogels for electrically responsive drug delivery, J. Control. Release 328 (2020) 192–209, https://doi.org/10.1016/j.jconrel.2020.08.051.
[7] K. Roshanbinfar, L. Vogt, B. Greber, S. Diecke, A.R. Boccaccini, T. Scheibel, F. B. Engel, Electroconductive biohybrid hydrogel for enhanced maturation and beating properties of engineered cardiac tissues, Adv. Funct. Mater. 28 (2018) 1803951, https://doi.org/10.1002/adfm.201803951.
[8] Q. Ge, Z. Chen, J. Cheng, B. Zhang, Y.-F. Zhang, H. Li, X. He, C. Yuan, J. Liu, S. Magdassi, S. Qu, 3D printing of highly stretchable hydrogel with diverse UV curable polymers, Sci. Adv. 7 (2021) eaba4261, https://doi.org/10.1126/sciadv.aba4261.
[9] R. Yang, Z. Guo, Z. Yu, F. Du, V.G.N. Thyagaraja, L. Lin, D.R. Yu, P. Xu, J. N. Armstrong, S. Lin, C. Zhou, J. Liu, 3D-printed conducting polymer hydrogel-based DC generator for self-powered electromechanical sensing, Nano Energy 117 (2023) 108857, https://doi.org/10.1016/j.nanoen.2023.108857.
[10] J.R. Greer, V.S. Deshpande, Three-dimensional architected materials and structures: design, fabrication, and mechanical behavior, MRS Bull. 44 (2019) 750–757, https://doi.org/10.1557/mrs.2019.232.
[11] J.U. Surjadi, L. Gao, H. Du, X. Li, X. Xiong, N.X. Fang, Y. Lu, Mechanical metamaterials and their engineering applications, Adv. Eng. Mater. 21 (2019) 1800864, https://doi.org/10.1002/adem.201800864.
[12] S. Peng, Y. Li, L. Wu, J. Zhong, Z. Weng, L. Zheng, Z. Yang, J.-T. Miao, 3D printing mechanically robust and transparent polyurethane elastomers for stretchable electronic sensors, ACS Appl. Mater. Interfaces 12 (2020) 6479–6488, https://doi.org/10.1021/acsami.9b20631.
[13] A. Nadernezhad, N. Khani, G.A. Skvortsov, B. Toprakhisar, E. Bakirci, Y. Menceloglu, S. Unal, B. Koc, Multifunctional 3D printing of heterogeneous hydrogel structures, Sci. Rep. 6 (2016) 33178, https://doi.org/10.1038/srep33178.

[14] X. Sui, H. Guo, C. Cai, Q. Li, C. Wen, X. Zhang, X. Wang, J. Yang, L. Zhang, Ionic conductive hydrogels with long-lasting antifreezing, water retention and self-regeneration abilities, Chem. Eng. J. 419 (2021) 129478, https://doi.org/10.1016/j.cej.2021.129478.
[15] Y. Jian, S. Handschuh-Wang, J. Zhang, W. Lu, X. Zhou, T. Chen, Biomimetic anti-freezing polymeric hydrogels: keeping soft-wet materials active in cold environments, Mater. Horiz. 8 (2021) 351–369, https://doi.org/10.1039/D0MH01029D.
[16] D. Chen, H. Bai, H. Zhu, S. Zhang, W. Wang, W. Dong, Anti-freezing, tough, and stretchable ionic conductive hydrogel with multi-crosslinked double-network for a flexible strain sensor, Chem. Eng. J. 480 (2024) 148192, https://doi.org/10.1016/j.cej.2023.148192.
[17] Y. Feng, S. Wang, Y. Li, W. Ma, G. Zhang, M. Yang, H. Li, Y. Yang, Y. Long, Entanglement in smart hydrogels: fast response time, anti-freezing and anti-drying, Adv. Funct. Mater. 33 (2023) 2211027, https://doi.org/10.1002/adfm.202211027.
[18] J. Liu, Z. Chen, Y. Chen, H.U. Rehman, Y. Guo, H. Li, H. Liu, Ionic conductive organohydrogels with dynamic pattern behavior and multi-environmental stability, Adv. Funct. Mater. 31 (2021) 2101464, https://doi.org/10.1002/adfm.202101464.
[19] Z. Wu, X. Yang, J. Wu, Conductive hydrogel- and organohydrogel-based stretchable sensors, ACS Appl. Mater. Interfaces 13 (2021) 2128–2144, https://doi.org/10.1021/acsami.0c21841.
[20] M. Criado-Gonzalez, A. Dominguez-Alfaro, N. Lopez-Larrea, N. Alegret, D. Mecerreyes, Additive manufacturing of conducting polymers: recent advances, challenges, and opportunities, ACS Appl. Polym. Mater. 3 (2021) 2865–2883, https://doi.org/10.1021/acsapm.1c00252.
[21] Q. Zhao, J. Liu, Z. Wu, X. Xu, H. Ma, J. Hou, Q. Xu, R. Yang, K. Zhang, M. Zhang, H. Yang, W. Peng, X. Liu, C. Zhang, J. Xu, B. Lu, Robust PEDOT:PSS-based hydrogel for highly efficient interfacial solar water purification, Chem. Eng. J. 442 (2022) 136284, https://doi.org/10.1016/j.cej.2022.136284.
[22] A. Dominguez-Alfaro, M. Criado-Gonzalez, E. Gabirondo, H. Lasa-Fernández, J. L. Olmedo-Martínez, N. Casado, N. Alegret, A.J. Müller, H. Sardon, A. Vallejo-Illarramendi, D. Mecerreyes, Electroactive 3D printable poly(3,4-ethylenedioxythiophene)-graft-poly(ε-caprolactone) copolymers as scaffolds for muscle cell alignment, Polym. Chem. 13 (2021) 109–120, https://doi.org/10.1039/D1PY01185E.
[23] A. Dominguez-Alfaro, E. Gabirondo, N. Alegret, C.M. De León-Almazán, R. Hernandez, A. Vallejo-Illarramendi, M. Prato, D. Mecerreyes, 3D Printable conducting and biocompatible PEDOT-graft-PLA copolymers by direct ink writing, Macromol. Rapid Commun. 42 (2021) 2100100, https://doi.org/10.1002/marc.202100100.
[24] B. Lu, H. Yuk, S. Lin, N. Jian, K. Qu, J. Xu, X. Zhao, Pure PEDOT:PSS hydrogels, Nat. Commun. 10 (2019) 1043, https://doi.org/10.1038/s41467-019-09003-5.
[25] W. Ge, S. Cao, Y. Yang, O.J. Rojas, X. Wang, Nanocellulose/LiCl systems enable conductive and stretchable electrolyte hydrogels with tolerance to dehydration and extreme cold conditions, Chem. Eng. J. 408 (2021) 127306, https://doi.org/10.1016/j.cej.2020.127306.
[26] H. Cai, D. Zhang, H. Zhang, M. Tang, Z. Xu, H. Xia, K. Li, J. Wang, Trehalose-enhanced ionic conductive hydrogels with extreme stretchability, self-adhesive and anti-freezing abilities for both flexible strain sensor and all-solid-state supercapacitor, Chem. Eng. J. 472 (2023) 144849, https://doi.org/10.1016/j.cej.2023.144849.
[27] Y. Zhang, K. Liu, T. Liu, C. Ni, D. Chen, J. Guo, C. Liu, J. Zhou, Z. Jia, Q. Zhao, P. Pan, T. Xie, Differential diffusion driven far-from-equilibrium shape-shifting of hydrogels, Nat. Commun. 12 (2021) 6155, https://doi.org/10.1038/s41467-021-26464-9.
[28] Z. Zhao, J. Wu, X. Mu, H. Chen, H.J. Qi, D. Fang, Origami by frontal photopolymerization, Sci. Adv. 3 (2017) e1602326.
[29] C.N. Bowman, C.J. Kloxin, Toward an enhanced understanding and implementation of photopolymerization reactions, AIChE J 54 (2008) 2775–2795, https://doi.org/10.1002/aic.11678.
[30] Y.-M. Huang, C.-P. Jiang, Curl distortion analysis during photopolymerisation of stereolithography using dynamic finite element method, Int. Journ. Adv. Manufac. Tech. 21 (2003) 586–595, https://doi.org/10.1007/s00170-002-1317-z.
[31] E. Fantino, I. Roppolo, D. Zhang, J. Xiao, A. Chiappone, M. Castellino, Q. Guo, C. F. Pirri, J. Yang, 3D Printing/Interfacial Polymerization Coupling for the Fabrication of Conductive Hydrogel, Macromol. Mater. Eng. 303 (2018) 1700356, https://doi.org/10.1002/mame.201700356.
[32] R.S. Jordan, J. Frye, V. Hernandez, I. Prado, A. Giglio, N. Abbasizadeh, M. Flores-Martinez, K. Shirzad, B. Xu, I.M. Hill, Y. Wang, 3D printed architected conducting polymer hydrogels, J. Mater. Chem. B 9 (2021) 7258–7270, https://doi.org/10.1039/D1TB00877C.
[33] H. Zhu, X. Hu, B. Liu, Z. Chen, S. Qu, 3D printing of conductive hydrogel-elastomer hybrids for stretchable electronics, ACS Appl. Mater. Interfaces 13 (2021) 59243–59251, https://doi.org/10.1021/acsami.1c17526.
[34] N. Lopez-Larrea, M. Criado-Gonzalez, A. Dominguez-Alfaro, N. Alegret, I. del Agua, B. Marchiori, D. Mecerreyes, Digital light 3D printing of PEDOT-based photopolymerizable inks for biosensing, ACS Appl. Polym. Mater. 4 (2022) 6749–6759, https://doi.org/10.1021/acsapm.2c01170.
[35] C. Zhang, H. Zheng, J. Sun, Y. Zhou, W. Xu, Y. Dai, J. Mo, Z. Wang, 3D Printed, solid-state conductive ionoelastomer as a generic building block for tactile applications, Adv. Mater. 34 (2022) 2105996, https://doi.org/10.1002/adma.202105996.
[36] X.-Y. Cheng, S.-Q. Peng, L.-X. Wu, Q. Sun, 3D-printed stretchable sensor based on double network PHI/PEDOT:PSS hydrogel annealed with cosolvent of H2O and DMSO, Chem. Eng. J. 470 (2023) 144058, https://doi.org/10.1016/j.cej.2023.144058.